Chapter 6

Volatile snowlines in embedded disks around low-mass protostars

Abstract. *Context*. Models of the young solar nebula assume that the disk is hot initially such that most volatiles are in the gas phase. Water emission arising from within 50 AU radius has been detected around low-mass embedded young stellar objects. The question remains whether an actively accreting disk can be warm enough to have gas-phase water up to 50 AU radius. No detailed studies have yet been performed on the extent of snowlines in an accreting disk embedded in a dense envelope (Stage 0).
Aims. Quantify the location of gas-phase volatiles in the inner envelope and disk system for an actively accreting embedded disk.
Methods. Two-dimensional physical and radiative transfer models have been used to calculate the temperature structure of embedded protostellar systems. The heating due to viscous accretion is added through the diffusion approximation. Gas and ice abundances of H_2O, CO_2, and CO are calculated using the density dependent thermal desorption formulation.
Results. The midplane water snowline increases from 5 to ~ 30 AU for accretion rates between 10^{-9}–10^{-4} $M_\odot$ yr^{-1}. CO_2 can remain in the solid phase within the disk for $\dot{M} \leq 10^{-5}$ $M_\odot$ yr^{-1} down to ~ 40 AU. CO is always in the gas phase for an actively accreting disk independent of disk properties and accretion rate. The predicted optically thin water emission is consistent with the detected water emission toward the Stage 0 embedded young stellar objects. An accreting embedded disk can only account for water emission arising from $R < 50$ AU, however, and drops rapidly for $\dot{M} \leq 10^{-5}$ $M_\odot$yr^{-1}. Thus, this extent can be tested with future ALMA observations.
Conclusion. Volatiles such as H_2O, CH_3OH, and CO_2 sublimate out to 30 AU in the midplane in young disks and, thus, can reset the chemical content inherited from the envelope. A hot young solar nebula out to 30 AU can only have occurred during the deeply embedded Stage 0, not during the T Tauri phase of our early solar system.

D. Harsono, S. Bruderer, E. F. van Dishoeck
in prep.

6.1 Introduction

The snowlines of various volatiles play a major role for planet formation. Beyond the snowline, the high abundances of solids allow for efficient sticking to form larger bodies. Thus, the amount of larger bodies is increased by the presence of ices (e.g. Stevenson & Lunine 1988; Ros & Johansen 2013). Extensive studies have investigated the snowline in protoplanetary disks around pre-main-sequence stars during which supposedly the solar system was formed (e.g. Lissauer 1987; Pollack et al. 1996). It is thought the early pre-solar nebula was (> 1500 K) such that both volatiles and refractories are in the gas phase (Cassen 2001; Scott 2007). This pushes the water snowline up to beyond a few AU radius. The evidences of such a hot solar nebula come from the history of the refractories, however the volatile content of comets seems to indicate that a part of the disk remains cold (see Pontoppidan et al. 2014). The evolution of the

snowline due to disk and star evolution and its accretion rate affect the chemical composition in the region relevant to planet formation (e.g., Lodders 2004; Davis 2005; Öberg et al. 2011b). The most relevant volatiles are the known major ice species, H_2O, CO_2, and CO. Observations and theoretical models of protoplanetary disks around pre-main sequence T-Tauri stars are not warm enough to have gas-phase volatiles in the midplane beyond 30 AU and for the case of H_2O, only a few AU (e.g., D'Alessio et al. 1998; Dullemond et al. 2007). Such high temperature at large radii could potentially only be achieved during the deeply embedded phase of star formation when the accretion rate is high. The question remains how hot can an embedded accreting disk become due to its high accretion rate ($\geq 10^{-6}\ M_\odot\ \mathrm{yr}^{-1}$, Dunham et al. 2014).

Spatially resolved warm water emission ($T_{\rm ex} \sim 120$ K, Persson et al. 2014) has been recently detected from within the inner 50 AU radius of several deeply embedded (Class 0) low-mass protostars (e.g., Jørgensen & van Dishoeck 2010b; Persson et al. 2012). These are very young objects whose envelope mass is substantially larger than the mass at smaller scales (also denoted as Stage 0, Robitaille et al. 2006). The emission is expected to arise from $T_{\rm dust} > 100$ K regions where the gas-phase water abundance is at its maximum (Fraser et al. 2001; Aikawa et al. 2008; Mottram et al. 2013). This inner region is, however, also where the disk forms (Larson 2003; Williams & Cieza 2011; Li et al. 2014). Rotationally supported disks (RSDs) have been detected recently around low-mass protostars (e.g., Tobin et al. 2012; Murillo et al. 2013). This paper studies the volatiles content in such embedded disks to investigate the location of their snowlines when the accretional heating is included.

Direct observational evidence of snowlines of the major ice species toward protoplanetary disks around pre-main sequence stars rely on the chemical changes that occur when a molecule is absent from the gas phase. The commonly observed snowline is that of CO through the detection of DCO^+ and N_2H^+ lines, which are both destroyed in reactions with CO (e.g. van Dishoeck et al. 2003; Guilloteau et al. 2006; Qi et al. 2008; Mathews et al. 2013; Qi et al. 2013). The CO snowline location with respect to water and CO_2 snowlines have direct impact on the amount of water present in giant planets atmospheres (Madhusudhan et al. 2011; Moses et al. 2013). The water snowline has been inferred to be within a few AU from direct observation of mid-infrared water lines (Pontoppidan et al. 2010; Zhang et al. 2013). Thus, significant progress has been made in identifying snowlines in protoplanetary disks in the later stages and their location with respect to gas giant formation (e.g., Kennedy & Kenyon 2008; Pontoppidan et al. 2014). Yet, the accretion process through the disk begins in the early stages of star formation at the time that the disk itself is forming. The amount of gaseous volatiles within embedded disks is, therefore, affected by their formation process which results in different chemical structures of the emerging protoplanetary disks (Visser et al. 2011). A related question centers whether these volatiles are 'inherited' or 'reset' during the planet formation process (Pontoppidan et al. 2014). The 'reset' scenario refers to the chemical processing of ices as the gas and dust are exposed to elevated temperatures (> 40 K) during their voyage from the envelope to the disk.

Water is the key volatile in star and planet formation; it is also the major constituent of ices on the grains that facilitate planet formation (Gibb et al. 2004; Öberg et al. 2011a) and a major coolant (Karska et al. 2013). Most of the water is formed during the pre-stellar stage, and then transported through the envelope into the disk and planets. Tracing the water history from early stages of star formation to planet forming regions hints at the origin of water in planets (van Dishoeck et al. 2014). The crucial step that is yet relatively unexplored is the processing of water during the disk formation process.

The water vapor content around protostars is investigated by the 'Water In Star-forming regions with Herschel' key program (WISH, van Dishoeck et al. 2011). Due to the large beam of *Herschel*, a significant fraction of the detected water emission is from the large-scale envelope

and the bipolar outflow (Kristensen et al. 2012; Herczeg et al. 2012; Mottram et al. 2014). More importantly, most of the detected water emission comes from water in the outflow that will escape the system and will not be retained by the disk. In order to determine the amount of water vapor associated with the inner envelope or disk, an isotopolog of warm water ($H_2^{18}O$) was observed toward a few low-mass embedded protostars. Visser et al. (2013) reported a detection of the $H_2^{18}O$ line (1096 GHz) with HIFI (de Graauw et al. 2010) toward the embedded protostar NGC 1333 IRAS2A. However, they found that the line is still optically thick with an emitting region of ~ 100 AU. Thus, it remains difficult to constrain the amount of water vapor in embedded disks with single-dish observations.

Although $H_2^{16}O$ line emission cannot be observed from the ground, except for masers, a few of the rotational transitions of its isotopologs are observable such as $H_2^{18}O$ and deuterated water (HDO). Furthermore, interferometric facilities such as the Plateau de Bure Interferometry (PdBI) and the Submillimeter Array (SMA) can spatially and spectrally resolve these lines. With those facilities, Jørgensen & van Dishoeck (2010a,b) detected $H_2^{18}O$ and HDO emission originating from within the inner 25 AU radius of a Class 0 low-mass protostar. More recently, spatially and spectrally resolved warm water emission has been detected toward four low-mass embedded protostars with the PdBI (Persson et al. 2012, 2013) and toward one high mass disk (van der Tak et al. 2006; Wang et al. 2012). From the kinematical information, both Jørgensen & van Dishoeck (2010b) and Persson et al. (2012) found that the water emission does not show Keplerian motion and concluded that it must be emitted from a flattened disk-like structure that is still dominated by the radial infalling motions.

This paper investigates snowlines of volatiles within an accreting disk embedded in a massive envelope. The spatial extent and the water vapor emission are compared with the observed values toward three deeply embedded protostars. The thermal structure of an actively accreting disk is computed including the additional heating due to the energy released from the viscous dissipation. Most previous studies of the thermal structure of an accreting disk focused on the later evolutionary stage of disk evolution where the envelope has largely dissipated away. Furthermore, they focused on the midplane temperature structure (e.g., Sasselov & Lecar 2000; Lecar et al. 2006; Kennedy & Kenyon 2008). This additional heating shifts the snowlines of volatiles outward to larger radii than in disks around pre-main sequence stars (Davis 2005; Garaud & Lin 2007; Min et al. 2011). The details of the physical and chemical structure of the embedded disk are presented in Section 6.2. Section 6.3 presents the snowlines location as function of disk and stellar properties. The results are compared with observations and discussed in Section 6.4. Section 6.5 summarizes the main results and conclusions.

6.2 Physical and chemical structures

6.2.1 Physical structure

A simple parametrized embedded disk (disk + flattened envelope) model is used to construct the density structure following Crapsi et al. (2008). The main parameters are disk mass ($M_{\rm disk}$) and disk radius ($R_{\rm disk}$). A number of parameters defining the envelope and the disk are fixed and summarized in Table 6.1. Through the combined continuum spectral energy distribution and submm continuum images modelling, the envelope masses toward the observed embedded sources (NGC1333 IRAS2A, IRAS4A, and IRAS4B) are found to be between 3 – 5 $M_\odot$ (Kristensen et al. 2012). For this purpose, the envelope mass is fixed at 1 $M_\odot$, which is appropriate for the objects from which the water emission has been detected (Jørgensen et al. 2009; Kristensen et al. 2012).

For the large-scale envelope, a flattened envelope due to rotation as described by Ulrich

Table 6.1 — Parameters for the embedded disk + envelope models. The varied parameters are indicated in boldface.

Variable [unit]	Description	Value(s)
$r_{\rm out}$ [AU]	Outer radius	10^4
$r_{\rm in}$ [AU]	Inner radius	0.1
$R_{\rm cen}$ [AU]	Centrifugal radius	200
$M_{\rm env}$ [$M_\odot$]	Envelope mass	1.0
$M_{\rm disk}$ [$M_\odot$]	**Disk mass**	0.05, 0.1, 0.2, 0.5
$R_{\rm disk}$ [AU]	**Disk radii**	50, 100, 200
H_0 [AU]	Scale height at 1 AU	0.2
$T_\star$ [K]	Stellar temperature	4000
$M_\star$ [$M_\odot$]	Stellar mass	0.5
$L_\star$ [$L_\odot$]	**Stellar luminosity**	1, 5, 8
$\dot{M}$ [$M_\odot$ yr^{-1}]	**Accretion rate**	$10^{-4,-5,-6,-7,-8,-9}$

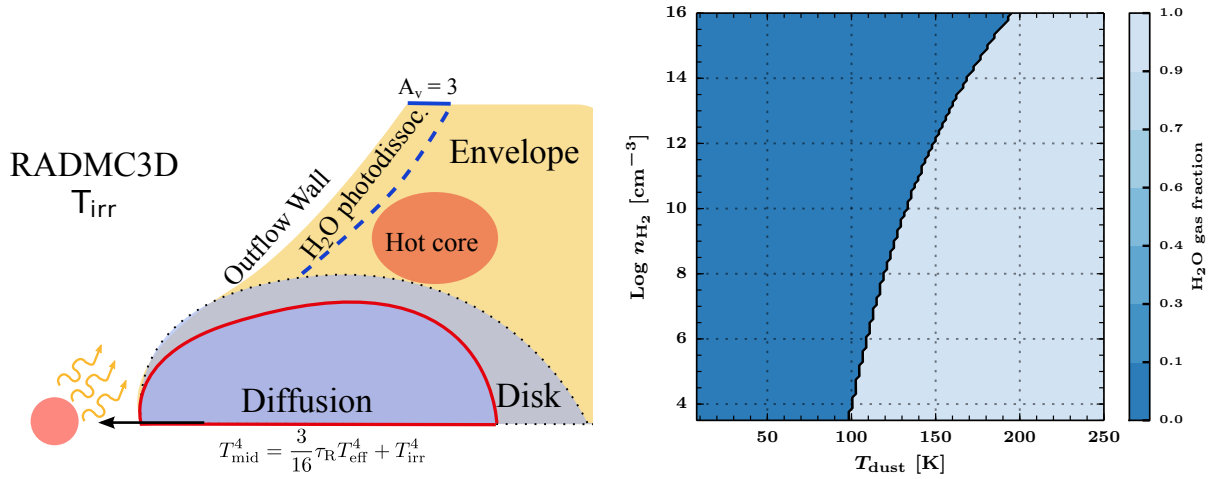

Figure 6.1 — *Left*: Schematic showing the calculation of the thermal structure of the disk by combining both the RADMC3D Monte Carlo simulation and the diffusion equation. The Monte Carlo simulation calculates the temperature structure due to the irradiation ($T_{\rm irr}$) from a central star while the diffusion equation is used to solve the temperature structure at high optical depths ($\tau_{\rm R} > 1$) as indicated by the red line. This high optical depth region starts typically below the disk surface. The outflow wall, classical hot core ($T_{\rm dust} > 100$ K) and photodissociation region are indicated. *Right*: Gas fraction ($n_{\rm gas}/n_{\rm gas} + n_{\rm ice}$) for $H_2^{16}O$ as a function of density and temperature.

(1976) is adopted whose densities are given by the following equation:

$$\rho_{\rm env}\left(r,\mu\right) \propto \left(\frac{R_{\rm cen}}{r}\right)^{1.5} \left(1+\frac{\mu}{\mu_0}\right)^{-1/2} \left(\frac{\mu}{2\mu_0}+\frac{R_{\rm cen}}{r}\mu_0^2\right)^{-1}, \tag{6.1}$$

where $\mu \equiv \cos\theta$, $R_{\rm cen}$ is the centrifugal radius, and r is the spherical radius. The centrifugal radius defines the region in which the material no longer flows radially and enters the disk. It is fixed at 200 AU, which corresponds to the maximum disk radius (~ 180 AU) observed toward a Class 0 embedded low-mass YSO (Murillo et al. 2013). For a given centrifugal radius, a particle follows a parabolic motion given by

$$\frac{r}{R_{\rm cen}}\frac{1-\mu/\mu_0}{1-\mu_0^2}=1, \tag{6.2}$$

where μ_0 satisfies the condition above at every r and μ. The outer radius of the envelope is fixed at $r_{\rm out}=10^4$ AU with an inner radius of 0.1 AU where the dust typically sublimates.

An outflow cavity is then carved out from the envelope density structure at $\mu_0 > 0.95$. Following Crapsi et al. (2008), the density inside the cavity is equal to that of the densities at $r_{\rm out}$. This creates a conical outflow with an aperture of 30° at large radii (semi-aperture of 15°). For a $1\ M_\odot$ envelope, gas densities $\sim 10^4$ cm^{-3} fill the envelope cavity, which is consistent with those observed toward YSOs (e. g, Bachiller & Tafalla 1999; Whitney et al. 2003)

A flared accretion disk is added to the envelope density structure. The density within the disk follows the power law dependence radially and has a Gaussian distribution vertically in z as expected from a hydrostatic disk. The flared disk densities (Shakura & Sunyaev 1973; Pringle 1981; Hartmann et al. 1998; Williams & Cieza 2011) are described by

$$\rho_{\rm disk}\left(R,z\right) = \frac{\Sigma(R/R_{\rm disk})^{-1}}{\sqrt{2\pi}H(R)} \exp\left[-\frac{1}{2}\left(\frac{z}{H(R)}\right)^2\right], \tag{6.3}$$

where H is the scale height fixed to 0.2 AU (H_0) at 1 AU (R_0), $R_{\rm disk}$ is the disk radius and R is the cylindrical radius. The radial dependence of the scale height is $H(R) = R\,H_0/R_0\,(R/R_0)^{2/7}$ (Chiang & Goldreich 1997). The densities are scaled with a constant factor such that the total disk mass is equal to the values in Table 6.1, distributed within the $R_{\rm disk}$. The total gas density in the model is $\rho = \rho_{\rm disk} + \rho_{\rm env}$ with a gas-to-dust mass ratio of 100.

6.2.2 Temperature structure and heating terms

The three-dimensional dust continuum radiative transfer code, RADMC-3D[1] is used to calculate the dust temperature structure. A 4000 K star characterized by 1, 5 and 15 $L_\odot$ is adopted (White & Hillenbrand 2004; Nisini et al. 2005). An accurate dust temperature structure of the disk is crucial in determining the location where various volatiles thermally desorb from the grain. This is difficult computationally for a massive optically thick disk being modelled here (see Min et al. 2009). Thus, we have separated the dust temperature calculations due to the central star irradiation (passive) from the viscous heating treatment (see Fig. 6.1 L). The former is determined by RADMC3D considering a black body central star as given in Table 6.1. The dust properties of Crapsi et al. (2008) are adopted and are composed of a distribution of ice coated silicates and graphite grains. The removal of ices from the grain at $T_{\rm dust} > 100$ K does not strongly alter the dust temperature structure.

[1]http://www.ita.uni-heidelberg.de/~dullemond/software/radmc-3d

An actively accreting disk provides additional heating from the loss of mechanical energy as the gas flows inward. The steady state accretion rate is typically between $10^{-5} - 10^{-7}$ $M_\odot$ yr^{-1} (Hueso & Guillot 2005). However, episodic accretion events such as those simulated by Vorobyov (2009) can have transient spikes with an accretion rate up to 10^{-4} $M_\odot$ yr^{-1}. Thus, disk accretion rates between 10^{-9}–10^{-4} $M_\odot$ yr^{-1} are adopted following the α disk formalism (Shakura & Sunyaev 1973; Williams & Cieza 2011). The viscous heating rate per volume is given by

$$Q_{\rm visc} = \frac{9}{4}\rho_{\rm disk} v \Omega^2, \tag{6.4}$$

where $v = \alpha c_{\rm s} H$ is the α dependent turbulent viscosity parameter, $c_{\rm s}$ is the sound speed of the gas, and Ω is the Keplerian angular velocity. At steady state, the viscosity is related to the disk mass and the accretion rate through (Lodato 2008):

$$\dot{M} = 3\pi v \Sigma. \tag{6.5}$$

To explore the amount of heating, the viscosity term v is varied for the explored accretion rates at a fixed disk mass. The effective temperature ($T_{\rm visc}$) associated with the total energy released at the inner radius assuming a hydrostatic disk is

$$\sigma_{\rm SB} T_{\rm visc}^4 (R) = \int Q_{\rm visc}(R)\, dz = \frac{3}{8\pi}\frac{GM_\star}{R^3}\dot{M}\left(1 - \sqrt{\frac{R_\star}{R}}\right). \tag{6.6}$$

This is obtained by integrating over the viscous heating terms vertically for each radius. Furthermore, $T_{\rm visc}$ is the effective temperature of the disk at the optically thin photosphere without the addition of stellar irradiation. However, the real temperature at the midplane of an active disk is proportional to the optical depth (Hubeny 1990): $T_{\rm mid}^4 \sim \kappa_{\rm R}\Sigma_{\rm gas} T_{\rm visc}^4$ with κ_R the Rosseland mean opacity which results in higher midplane temperatures. Such a method is similar to that of Kennedy & Kenyon (2008) and Hueso & Guillot (2005) in the optically thick regime. Note that the heating from the accreting disk is caused by dissipation of energy of both gas and dust. To account for the irradiation from the accreting disk, $L_{\rm visc} = \int \pi\sigma T_{\rm visc}(R)^4 R dR$ is added to the central luminosity $L_\star$ by determining its blackbody spectrum at $T_{\rm visc}$ at all radii.

The following steps are taken to calculate the dust temperature of an accreting embedded disk.

- Monte Carlo dust continuum radiative transfer is used to simulate the photon propagation to determine the passively heated dust temperature structure ($T_{\rm irr}$) due to the stellar luminosity ($L_\star + L_{\rm visc}$).
- Viscous heating is added to the region of the disk where $\tau_{\rm R} > 1$. This is done by fixing the midplane temperatures to $T_{\rm mid} = \left(\frac{3}{16}\kappa_{\rm R}\Sigma_{\rm gas}T_{\rm visc}^4 + T_{\rm irr}^4\right)^{1/4}$. The vertical dust temperature structure is calculated using the diffusion approximation $\nabla D \nabla T^4 = 0$ bounded by $T_{\rm irr}$ at the surface and $T_{\rm mid}$ at the midplane where $D = (3\rho_{\rm dust}\kappa_{\rm R})^{-1}$. The diffusion is performed within the $\tau_{\rm R} > 1$ regions.

The addition of the viscous heating can increase the dust temperatures to > 2000 K. The typical dust vaporization temperature is ~ 1500 K, therefore, we have limited the dust temperature to 1500 K. Gas opacities in the inner disk is not taken into account, which will affect the exact temperature in that region. This does not change the location of the snowlines since they are defined by dust temperatures $T_{\rm dust} \leq 160$ K.

The snowlines of protoplanetary disks without an envelope were obtained (see Fig. 6.8) and compared with Min et al. (2011) to verify our approach. Using this formulation, the differences in predicted water snowlines are typically within 2 AU at high accretion rates.

6.2.3 Molecular abundances

The aim of this paper is to calculate the 2D snowlines or snow 'surfaces' for CO, CO_2, and $H_2^{16}O$ in embedded disks. The region in which these volatiles freeze-out onto grains depends on the temperature and density structure. At steady state, the rate at which the molecule is adsorbed on the grain, $\mathcal{R}_{\rm ads}$, is balanced by the thermal desorption rate, $\mathcal{R}_{\rm des}$. The adsorption rate is given by

$$\mathcal{R}_{\rm ads} = n_{\rm X} n_{\rm dust} \pi a_{\rm dust}^2 \sqrt{3 k_{\rm B} T_{\rm gas}/m_{\rm X}}, \tag{6.7}$$

where $m_{\rm X}$ is the molecular mass, $n_{\rm X}$ is the number density of the molecule, $T_{\rm gas}$ is the gas temperature, $n_{\rm dust} = 10^{-12}\, n_{\rm H}$ is the dust number density (Visser et al. 2009) with $a_{\rm dust} = 0.1$ μm as the effective grain size, and $k_{\rm B}$ is the Boltzmann constant. The thermal desorption rate is

$$\mathcal{R}_{\rm thdes} = 4\pi a_{\rm dust}^2 n_{\rm dust} \nu_1 \exp(-E_{\rm b}/k_{\rm B} T_{\rm dust}) \xi, \tag{6.8}$$

where ν_1 is the first-order pre-exponential factor as calculated from the binding energy, $E_{\rm b}$ (Hasegawa et al. 1992; Walsh et al. 2010)

$$\nu_1 = \sqrt{\frac{2 N_{\rm ss} E_{\rm b}}{\pi^2 m_{\rm X}}}\ {\rm s}^{-1} \tag{6.9}$$

with the number of binding sites, $N_{\rm ss}$ taken to be 8×10^{14} cm^{-2} for a 0.1 μm grain following Visser et al. (2011), and $T_{\rm dust}$ the dust temperature. A dimensionless factor ξ is used to switch between zeroth order to first order desorption when the ice thickness is less than a monolayer:

$$\xi = \frac{n_{\rm ice}}{\max(n_{\rm ice}, N_{\rm b} n_{\rm dust})} \tag{6.10}$$

with $N_{\rm b} = 10^6$ the number of binding sites per dust grain. The properties for each molecule are given in Table 6.2 along with the calculated pre-exponential factor ν_1. These binding energies assume pure ices. Figure 6.1 (R) shows an example of the gas fraction for water at different densities and temperatures. At steady state, the number density of solids of species X is simply given by

$$\frac{n_{\rm ice}}{n_{\rm gas}} = \frac{n_{\rm dust} \pi a_{\rm dust}^2 \left(3 k_{\rm B} T_{\rm gas}/m_X\right)^{1/2}}{\nu_1 \exp\left(-E_{\rm b}/T_{\rm dust}\right) \xi}. \tag{6.11}$$

The typical timescales for adsorption are $4 - 6 \times 10^3$ year at temperature of 50 K and number densities of 10^6 cm^{-3}. This implies that the steady state assumption is not valid at lower densities present in the large-scale envelope ($r > 1000$ AU) where the freeze-out timescales becomes longer than the lifetime of the core (e.g., Jørgensen et al. 2005). On the other hand, this paper focuses on the gas phase abundances at small-scales $r \leq 100$ AU where the number densities are $n_{\rm H} > 10^6$ cm^{-3}. Photodesorption can be ignored at such high densities and within the disk, but it may be important at the disk's surface and along the outflow cavity wall. Since the water vapor will also be rapidly photodissociated in those locations, these regions are not major water reservoirs (see Fig. 6.1 L). To approximate this region, water is assumed not to be present within a region that is characterized by $A_{\rm V} \leq 3$ or $N_{\rm H} \leq 6 \times 10^{21}$ cm^{-2}. A more detailed gas phase abundance structure through a chemical network will be explored in the future.

Table 6.2 — Molecular parameters to calculate $\mathcal{R}_{\rm des}$.

Molecule	$\nu_1^{\rm a}$ [s^{-1}]	$E_{\rm b}$ [K]	Refs.
CO	6.4×10^{11}	855	Bisschop et al. 2006
CO_2	8.2×10^{11}	2400	Burke & Brown 2010
$H_2^{16}O$	2.1×10^{12}	5773	Fraser et al. 2001

[a] First order desorption pre-exponential factor calculated from the binding energies.

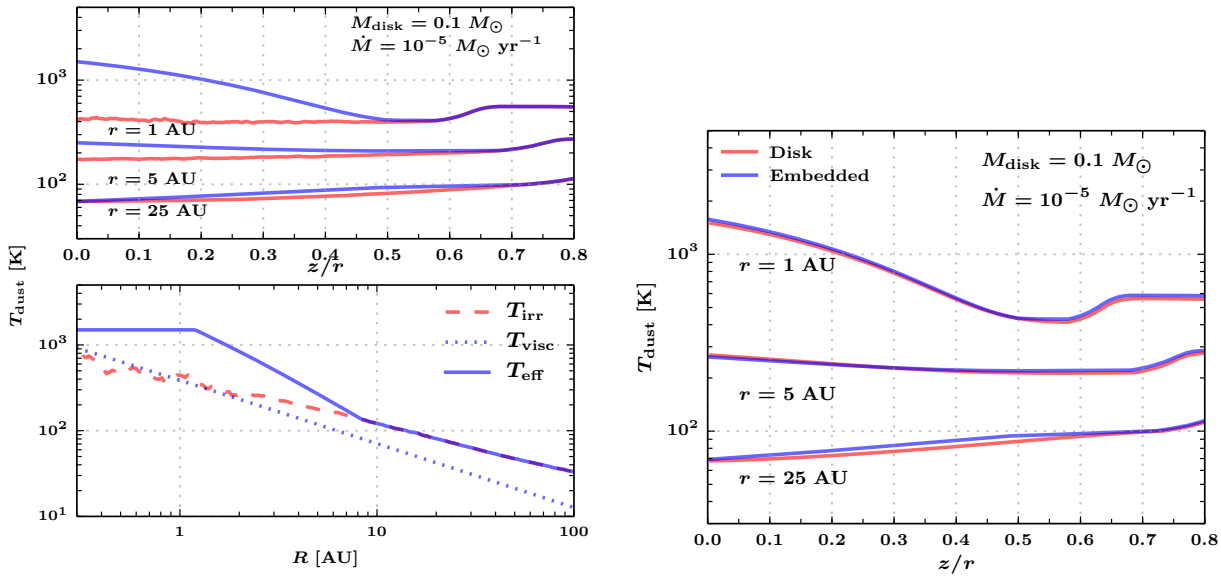

Figure 6.2 — *Left*: Midplane radial (*bottom*) and vertical temperatures (*top*) at 1, 5, and 25 AU for a $0.1\ M_\odot$ disk and an accretion rate of $10^{-5}\ M_\odot\ {\rm yr}^{-1}$. The red dashed (*bottom*) and solid (*top*) lines indicate the thermal structure of a passively irradiated disk ($T_{\rm irr}$) calculated by the Monte Carlo simulation. The blue solid lines indicate the temperatures including the viscous heating ($T_{\rm eff} = \left(\frac{3}{16}\kappa_{\rm R}\Sigma_{\rm gas}T_{\rm visc}^4 + T_{\rm irr}^4\right)^{1/4}$). The viscous temperature as calculated from Eq. 6.6 is indicated by the dotted blue lines. *Right*: Comparison of the vertical temperature structure at 1, 5 and 25 AU between a protoplanetary disk (*red*) and an embedded disk (*blue*). The envelope mass is $1\ M_\odot$ for the embedded disk model. *Right*: Comparison of the vertical temperature structure at 1, 5 and 25 AU between a protoplanetary disk (*red*) and an embedded disk (*blue*). The envelope mass is $1\ M_\odot$ for the embedded disk model.

6.3 Results

6.3.1 Thermal structure of an actively accreting embedded disk

The locations at which various molecules can thermally desorb from the dust grain depend on the temperature structure of the disk. Irradiated disks have a warm upper layer with a cooler midplane. Figure 6.2 (red dashed lines) shows the midplane (*bottom*) and vertical (*top*) temperature at a number of radii for an embedded disk passively irradiated by a $1\ L_\odot$ central source. Here, we present the results for a $0.1\ M_\odot$ disk embedded in a $1\ M_\odot$ envelope (Fig. 6.2 left top). This result is also compared with a disk without any envelope in Fig. 6.2 (R). The difference is small in the inner disk, and lies primarily at large radii where the midplane temperature structure ($T_{\rm mid} \propto \Sigma$) is weakly affected by the adopted envelope model. Even at $r > 25$ AU, the difference is small since the centrifugal radius of the envelope is defined at 200 AU. This results in density pile-up, which is responsible for the increase of temperature, at 200 AU. A more flattened envelope model ($R_{\rm c} \sim 50$ AU) will result in a larger difference in the temperature. The

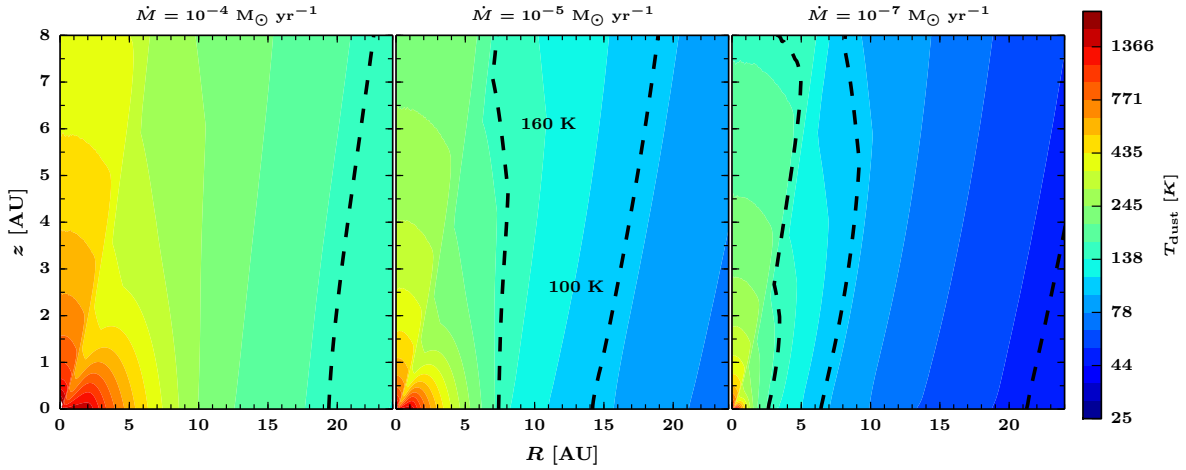

Figure 6.3 — Dust temperature structure in the inner 24 AU for three different accretion rates for a 0.1 $M_\odot$ disk embedded in a 1 $M_\odot$ envelope. A 1 $L_\odot$ central heating source is adopted for these models. The two dashed lines indicate the 160 K and 100 K contours, which are important for the water snowlines.

inner few AU are highly optically thick at the peak wavelength of the central source such that few photons reach these regions. This does not affect the exact location of the snowline since $T >> T_{\rm desorb}$ as indicated in Fig. 6.1 (R) for water.

The temperatures of an actively accreting disk are indicated by the blue lines in Fig. 6.2. The dotted line shows the viscous temperature ($T_{\rm visc}$) as expected at the photosphere (optically

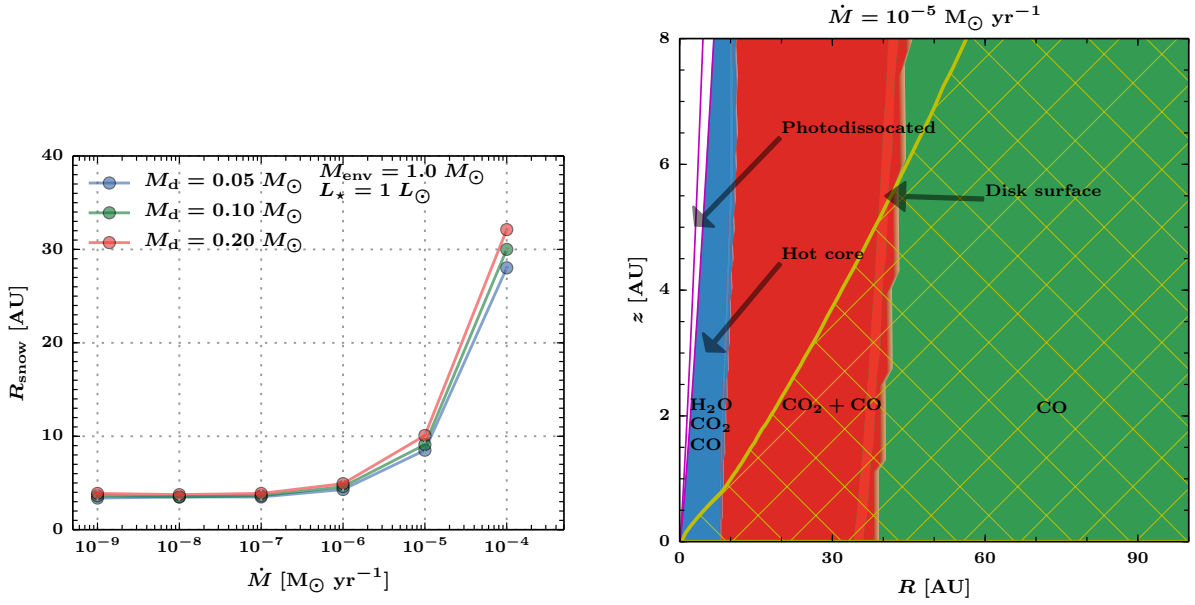

Figure 6.4 — *Left*: Midplane water snowlines as function of accretion rates and disk mass for a 200 AU disk. The different colors indicate the snowlines dependence on disk mass at a fixed stellar luminosity and envelope mass. *Right*: Locations of gas phase volatiles in the 0.1 $M_\odot$ disk embedded in a 1 $M_\odot$ envelope. The different colors indicate the different volatiles: water ($H_2^{16}O$, blue), CO_2 (red), and CO (green). The species that are in the gas phase within each region are all indicated. The accretion rate is indicated at the top. Three different regions are highlighted: photo-dissociation region defined by $A_{\rm V} = 3$, hot core, and the disk surface (yellow line assuming $T_{\rm gas} = T_{\rm dust}$).

thin) while the solid blue lines show the effective dust temperature corrected for optical depth and passive irradiation. As previously found, the addition of viscous heating can raise the temperatures in the inner few AU to > 1000 K (e.g., Calvet et al. 1991; D'Alessio et al. 1997; Davis 2005). The 2D dust temperature structure in the inner 20 AU is shown in Fig. 6.3 for three different accretion rates. The disk temperature is above 100 K up to ≥ 10 AU for an accretion rate of 10^{-5} $M_\odot$ yr^{-1}. As noted in Eq. 6.6, the viscous temperature depends on stellar mass (0.5 $M_\odot$) and the accretion rate through the disk (see Kennedy & Kenyon 2008). In addition, the effective temperature within the disk depends on the disk mass through Σ and the central luminosity ($L_\star$). Due to the R^{-3} dependence, the viscous heating is dominant in the inner few AU as indicated in Fig. 6.2 (*left bottom*). Consequently, the passive irradiation due to the central luminosity dominates the temperatures along the disk's photosphere and the outflow cavity wall while the viscous dissipation dominates the heating deep within the disk.

6.3.2 Water snowline

Using the obtained dust temperatures, the gas and ice number densities are calculated at each cell. To determine the snowline, the total available water mass is calculated adopting a water abundance of 10^{-4} with respect to H_2. The total available mass is then multiplied by the gas fraction to determine the total gas mass. The snowline is defined as the radius at which 50% of the total available water has frozen onto the grains ($M_{\rm gas}/M_{\rm ice} = 0.5$) (e.g., Min et al. 2011). This typically occurs at ∼160 K at high density regions ($n_{\rm H} \sim 10^{14}$ cm^{-3}, see dashed line in Fig. 6.3).

Figure 6.4 (L) presents the midplane snowline radius as a function of accretion rate. In the absence of accretion heating, the water snowline is located at ~ 5 AU. This does not strongly depend on the accretion rate until a value of $\dot{M} > 10^{-7}$ $M_\odot$ yr^{-1} is reached. The maximum water snowline is ~ 30 AU at an accretion rate of 10^{-4} $M_\odot$ yr^{-1}. The water snowline does not depend strongly on disk mass: it is located at only slightly smaller radius for a less massive disk as indicated in Fig. 6.4 (L).

The steep increase of the water snowline at high accretion rates can be understood by comparing the stellar luminosity with the accretion luminosity. The irradiating central luminosity is 1 $L_\odot$. The accretion luminosity is estimated by integrating Eq. 6.6 radially over the active disk between 0.1 and 200 AU in this case and is approximately $L_{\rm acc} \sim 0.5 \times GM_{\rm star}\dot{M}/R_{\rm in}$. Thus, the accretion luminosity is equal to that of the central star for $\dot{M} \sim 3 \times 10^{-6}$ $M_\odot$ yr^{-1}. For a central luminosity of 1 $L_\odot$, the accretion luminosity starts to contribute to the heating at $\dot{M} > 10^{-7}$ $M_\odot$ yr^{-1}.

The observable water emission depends on the water vapor column density. The water vapor column extends somewhat further than the snowline due to the vertical gradient in water vapor abundance. The available water is rapidly frozen out onto dust grains beyond the snowline. To determine whether the location of the snowline is within the disk or not, the hydrostatic disk surface is calculated through $H = c_{\rm s}/\Omega_{\rm K}$ where $c_{\rm s} = \sqrt{k_{\rm B}T_{\rm mid}/\mu m_{\rm H}}$ is the sound speed and $\Omega_{\rm K}$ is the Keplerian angular frequency. This is the approximated regime where the gas should be in Keplerian motion. For a 1 $L_\odot$ central star, most of the water emission arises from the classical hot core region above the hydrostatic disk surface as shown by the yellow line in Fig. 6.4 (R) if a constant water abundance of 10^{-4} with respect to H_2 is adopted.

6.3.3 CO and CO_2 snow lines

Pure CO_2 and CO ice thermally desorb from the dust grain over a narrow range of dust temperatures between 40–80 K and 15–30 K, respectively depending on the pressure (see Fig. 6.9 in the appendix). Due to their lower binding energies relative to water, CO and CO_2 are in the gas

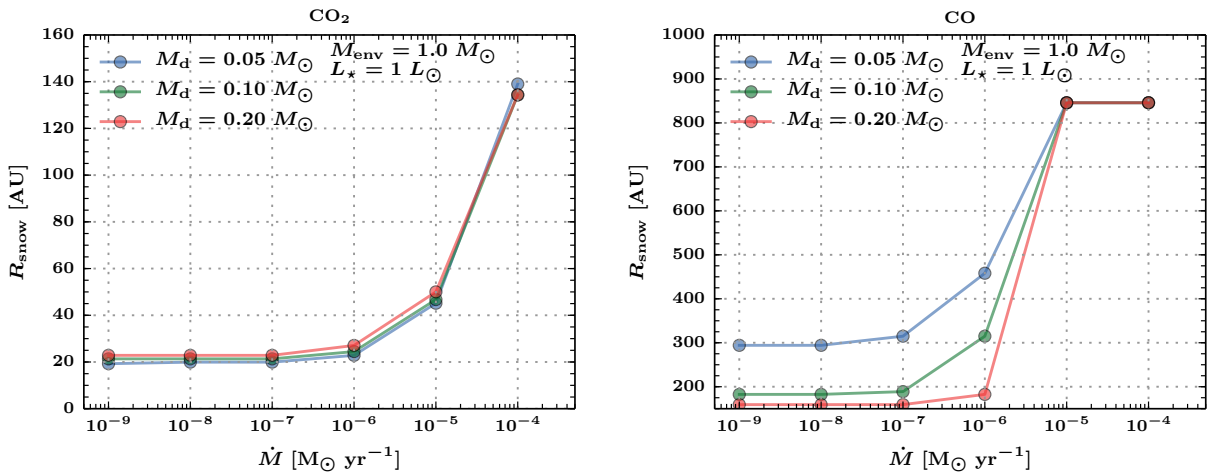

Figure 6.5 — *Left*: Midplane CO_2 snowlines as a function of accretion rates and disk mass for a 200 AU disk. *Right*: Midplane CO snowlines as a function of accretion rates for the same disk. The different colors indicate the snowlines dependence on disk mass at a fixed stellar luminosity (1 $L_\odot$) and envelope mass (1 $M_\odot$).

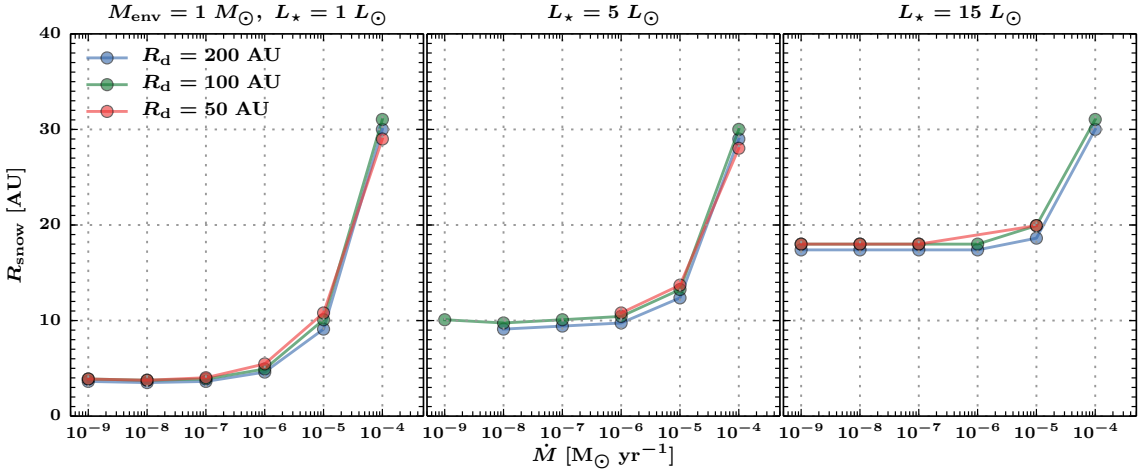

Figure 6.6 — Midplane water snowline as a function of stellar luminosity, accretion rate, and disk radius. The envelope mass is fixed at 1 $M_\odot$ with a disk mass of 0.1 $M_\odot$. The different panels show the water snowline as a function of stellar luminosity: 1 $L_\odot$ (*left*), 5 $L_\odot$ (*center*), and 15 $L_\odot$ (*right*). The different colors indicate the disk radius: 200 AU (*blue*), 100 AU (*green*), and 50 AU (*red*).

phase within a large part of the embedded disk. The CO_2 snowline is between 15–120 AU for 10^{-9}–10^{-4} $M_\odot$ yr^{-1} accretion rates. Thus, the entire disk including the midplane lacks of CO_2 ice for high accretion rates ($\dot{M} \sim 10^{-4}$ $M_\odot$ yr^{-1}). The snowline is located at ~20 AU for a more massive disk with lower accretion rates. The steep rise of the CO_2 snowline at high accretion rates is similar to that of water as shown in Fig. 6.5.

Since the adopted binding energy of CO is significantly lower than that of the other two molecules, CO largely remains in the gas phase within the disk for $L_\star \geq 1\ L_\odot$ independent of the accretion rate (see Fig. 6.5 right). At low accretion rates, the snowline is located at ~ 150 AU at the midplane indicating the presence of CO ice between 150 to 200 AU within the disk. However, the bulk of CO within the disk remains in the gas phase as shown in Fig. 6.4 (R). A smaller disk during the embedded phase would lead to stronger envelope irradiation (e.g.

D'Alessio et al. 1997), and, consequently, CO is not frozen out within the disk. A sufficiently large and massive disk ($M_{\rm disk} > 0.2\ M_\odot$ irradiated by a 1 $L_\odot$ star) could contain a larger fraction of CO ice at large radii. This is simply due to the increase of optical depth and, thus, lower dust temperatures at large radii.

6.3.4 Dependence on stellar and disk properties

Previous sections presented the vapor content for a $0.1\ M_\odot$ embedded disk surrounded by a 1 $M_\odot$ envelope irradiated by a 1 $L_\odot$ central star. As noted in Section 6.2.2, the effective midplane temperature ($T_{\rm eff}$) depends on the disk mass but an increasing disk mass leads to only a small change to the water snowline as shown in Fig. 6.4 (L). Figure 6.4 (R) shows that the water vapor can be either within the disk or within the hot core. The temperature along the outflow cavity wall is controlled by the central luminosity while the effective temperature deep inside the disk is proportional to its mass at a fixed accretion rate. This section investigates how the vapor content depends on disk radius and central luminosity at a fixed envelope and disk mass.

Figure 6.6 presents the locations of water snowline as a function of accretion rate, luminosity and disk radius. For a given disk structure, a factor of 5 increase in luminosity increases the midplane water snowline by a factor of 2 from 5 AU to ~ 10 AU at low accretion rates ($\dot{M} < 10^{-7}\ M_\odot$ yr^{-1}). A factor of 15 increase in luminosity yields a factor of ~ 4 increase at the location of the water snowline. A decreasing disk radius does not affect the midplane water snowline until the accretion luminosity starts to significantly contribute to the total luminosity. Thus, an increasing stellar luminosity ($L_\star$) has a greater effect on the midplane water snowline. This leads to a greater amounts of water vapor in the hot core (see Fig. 6.4 R) at low accretion rates. However, there is no change in terms of the water snowline location at high accretion rates ($\dot{M} > 10^{-5}\ M_\odot$ yr^{-1}) since the total luminosity is dominated by the accretion luminosity for these scenarios.

The CO_2 midplane snowline shows similar behavior as the water snowline (Fig. 6.10). It is in the gas phase at $R > 40$ AU for $L \geq 5\ L_\odot$. However, the CO_2 snowline shows a stronger dependence on the disk radius than that of water. For the high luminosity case $L_\star = 15\ L_\odot$, the CO_2 snowline increases from 40 AU to 80 AU as the disk radius increases from 50 AU to 200 AU. The CO midplane snowline depends on the disk radius for the 1 $L_\odot$ case (Fig. 6.11). Its location (> 500 AU) no longer depends on accretion rate for $L \geq 5 L_\odot$ for the adopted disk and envelope parameters. Thus, CO remains in the gas phase within the disk for $L \geq 5 L_\odot$.

6.4 Discussion

6.4.1 Comparison with previous results

In the absence of an envelope, similar stellar parameters and an accretion rate of $10^{-8}\ M_\odot$ yr^{-1} lead to the midplane water snowline located at ~ 1 AU (e.g., Sasselov & Lecar 2000) while our water snowline is located at ~ 3 AU (see Fig. 6.8). Lecar et al. (2006) suggest that the snowline can move out by increasing the accretion rate, disk mass and the dust opacities. The differences between the derived snowlines are unlikely to be due to the differences in radiative transfer treatment. Garaud & Lin (2007) also derived similar water snowlines to that of Min et al. (2011) (1 AU vs 2 AU) using different methods in deriving the dust temperatures and different opacities for similar accretion rates. The later takes into account the 2D vertical structure of the disk in detail. As Min et al. (2011) shows, most of the differences are due to the adopted dust opacities. Our value is 1 AU larger than the values tabulated in Min et al. (2011) adopting different dust opacity table. Furthermore, most of the previous studies adopt the minimum mass solar nebula (MMSN) model where $\Sigma \propto R^{-1.5}$ instead of the R^{-1} 2D parametric model

used in this paper (see e.g., Andrews et al. 2009). At the same accretion rate, the water snowline is at ~ 5 AU with the adopted disk embedded in a massive envelope models.

6.4.2 Caveats

The effect of convection in vertical direction is not included in this study. It is typically found to be important in the case of high accretion rates ($\dot{M} > 10^{-6}$ $M_\odot$ yr^{-1}, D'Alessio et al. 1998, Min et al. 2011). Convection is found to cool the midplane temperatures at $T_{\rm dust} > 500$ K. Thus, this should not affect the water (100–160 K), CO_2 (~ 50 K) and CO (~ 20 K) snowlines.

Under the assumption of the steady state accretion disk model, the typical values of $\alpha > 1$ is obtained for the case of an accretion rate of $\dot{M} = 10^{-4}$ $M_\odot$ yr^{-1}. This is significantly higher than that expected from magnetorotational instability (MRI) driven accretion in a MHD disk ($\alpha = 0.01$, Balbus & Hawley 1998). King et al. (2007) indicated that α could be ~ 0.4 for disks around compact systems. Such a high value of α in our models are obtained since we have fixed the density distribution for a high accretion rate. In reality, such a disk is unphysical. However, this is only encountered for the highest accretion rate of 10^{-4} $M_\odot$ yr^{-1}. Such a high accretion rate is expected to occur for a very short time. Furthermore, this paper explores the effect of the adopted accretion rates and disk masses for a given fixed parameters. Self-consistent models should be explored in details in the future.

An additional heating term that is not included is the magnetospheric shock (Calvet & Gullbring 1998). For the case of high accretion rates, it is expected that the accretion proceeds straight onto the star instead of stopping at $R_{\rm in}$. The luminosity that it generates is given by

$$L_{\rm acc} = \frac{GM_\star \dot{M}}{2R_\star}. \tag{6.12}$$

An accretion rate of 3×10^{-7} $M_\odot$ yr^{-1} will produce a shock luminosity equal to that of 1 $L_\odot$. Thus, the magnetospheric shock luminosity is expected to be one order of magnitude higher than that of the accretion luminosity from the disk at a fixed accretion rate irradiated by a 1 $L_\odot$ central star. Currently, this is not included in the total luminosity as emitted by the central star. On the other hand, this is similar to the results with a higher central luminosity of 15 $L_\odot$. The qualitative effect on the water snowline with the inclusion of magnetospheric shock can be explored by comparing the results at two different luminosities at a fixed accretion rate (see Sect 6.3.4).

6.4.3 Comparison with observations

The extent of the observed spatially resolved water emission toward low-mass embedded YSOs is between 25–90 AU (Jørgensen & van Dishoeck 2010b; Persson et al. 2012, 2014). The water snowline is weakly affected by the envelope properties investigated here. The maximum midplane water snowline in our models is ~ 30 AU with a disk mass of 0.1 $M_\odot$ with $R_{\rm disk} = 200$ AU and an accretion rate of 10^{-4} $M_\odot$ yr^{-1}. Thus, our results indicate that most of the water emission at $R < 50$ AU would originate from the combine disk and hot core if accretion rates can indeed be this high (see Fig. 6.4 R).

The amount of water vapor in the embedded disk models can be compared to the observed optically thin millimeter water emission toward deeply embedded YSOs. Thermalized $H_2^{18}O$ emission at 203.4 GHz ($3_{1,3} - 2_{2,0}$) is calculated using the following equation

$$I_\nu \approx B_\nu\,(T_{\rm ex})\,(1 - e^{-\tau}), \tag{6.13}$$

$$\tau = \frac{\bar{N}}{\mathcal{Q}\,(T_{\rm ex})\,\Delta V}\,\frac{A_{\rm ul} c^3}{8\pi\nu^3}\,e^{h\nu/k_{\rm B}T_{\rm ex}}, \tag{6.14}$$

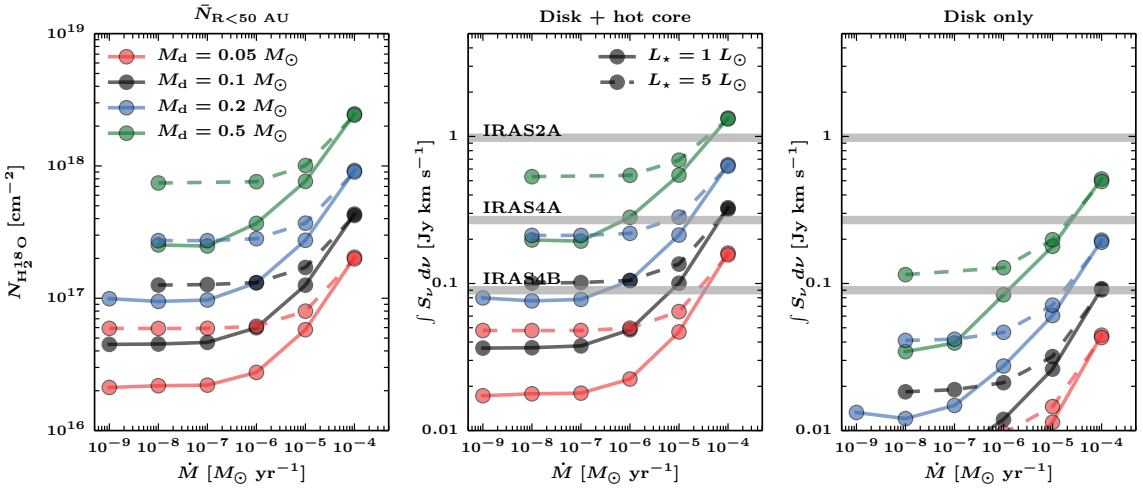

Figure 6.7 — *Left:* Beam averaged water ($H_2^{18}O$) column densities within 50 AU radius as a function of accretion rates. The different colors indicate the disk mass dependence: $M_d = 0.05\ M_\odot$ (red), 0.1 (black), 0.2 (blue) and 0.5 (green). The different lines show the luminosity dependence: $L_\star = 1\ L_\odot$ (solid) and 5 $L_\odot$ (dashed). *Center:* Integrated line flux densities assuming a Gaussian linewidth of 1 km s^{-1} which is appropriate for NGC1333-IRAS4B. The observed integrated $H_2^{18}O$ line is indicated by the gray lines for the three different embedded YSOs in Persson et al. (2014). *Right:* Integrated line flux densities arising from the disk only as defined by the yellow line in Fig. 6.4 (R).

where A_{ul} is the Einstein A coefficient of the 203 GHz transition is 4.5×10^{-7} s^{-1}, T_{ex} is taken to be 150 K, $E_u = 204$ K is the upper energy level, $g_u = 7$ is the weight of the upper level, and $\mathcal{Q}$ is the temperature dependent partition function adopted form the HITRAN database (Rothman et al. 2009). The beam averaged column density ($\bar{N}$) is taken from within 50 AU radius with ^{16}O:^{18}O isotopic ratio of 540 (Wilson & Rood 1994). The line profile is assumed to be Gaussian with a $FWHM$ (Δv) = 1–4 km s^{-1} as observed toward the three embedded sources reported by Persson et al. (2014).

Figure 6.7 (*left*) presents the mean $H_2^{18}O$ column density as a function of accretion rate for different disk masses and stellar luminosities. The mean column density rises sharply for $\dot{M} > 10^{-7}\ M_\odot$ as expected for a 1 $L_\odot$ stellar luminosity while it is shifted to $\dot{M} > 10^{-6}\ M_\odot$ for a 5 $L_\odot$ irradiating source. The typical line optical depth at the line center ($v = 0$ km s^{-1}) can be up to $\tau \geq 1$. The typical average column densities of water between 50 AU to 1000 AU are > 4 orders of magnitude lower than the values in Fig. 6.7. Thus, the water present within 50 AU dominates the total water mass for the adopted models.

The expected integrated $H_2^{18}O$ $3_{1,3}$–$2_{2,0}$ (203.4 GHz) line flux densities for the embedded disk models are also shown in Fig. 6.7 (*right*). The plotted integrated line flux densities are calculated with a Gaussian line profile with $\Delta v = 1$ km s^{-1} ($1.06 S_{v=0} \times \Delta V$ where $S_{v=0}$ is the peak flux density at line center) as observed toward NGC1333-IRAS4B (Persson et al. 2014). The observed line widths toward IRAS2A and IRAS4A are 4 and 3 km s^{-1}, respectively. Increasing Δv slightly increases the model integrated line flux densities.

The predicted integrated line flux densities from actively accreting embedded disk models are consistent with that observed toward NGC1333 IRAS4B if $M_d \leq 0.2\ M_\odot$ with $\dot{M} \sim 3 \times 10^{-7}\ M_\odot$ yr^{-1} for $L = 1\ L_\odot$. Jørgensen et al. (2009) estimated from the continuum that the disk mass is $\sim 0.2\ M_\odot$, which is consistent with our results. Decreasing the disk mass implies a higher accretion rate is required to reproduce the observed water emission. A higher accretion rate ($\sim 5 \times 10^{-5}\ M_\odot$ yr^{-1}) with lower disk mass is also consistent with the observed

extent of water emission at ~ 20 AU. A similar conclusion is reached for the case of IRAS4A whose disk is estimated to be $\sim 0.5\ M_\odot$ (Jørgensen et al. 2009). At these accretion rates, the accretion luminosity is of the order of the adopted central luminosity ($1\ L_\odot$). Since the bolometric luminosity toward NGC1333 IRAS4A and IRAS4B are a factor of 4–9 higher than the adopted central luminosity, a model with a factor of 2 lower mass disk can also reproduce the observed flux density. With such a lower mass disk, the hot core is the dominant source of emission instead of the Keplerian disk.

IRAS2A shows stronger integrated line emission (~ 1 Jy km s^{-1}) relative to the other 2 sources extending up to 90 AU radius. As pointed out above, a disk cannot be responsible for any warm water emission at $R > 50$ AU. Furthermore, Brinch et al. (2009) and Jørgensen et al. (2009) estimated that the disk is at most $\sim 0.05\ M_\odot$, which lowers the expected disk's contribution to the observed water emission. There are two possible scenarios that can explain such a high water emission: a more luminous star ($L_\star > 10\ L_\odot$) or an extremely high accretion rate ($> 10^{-4}\ M_\odot$ yr^{-1}). The former is consistent with the high bolometric luminosity of IRAS2A ($L_{\rm bol} = 35.7\ L_\odot$, Kristensen et al. 2012). In this case, most of the water emission arises from the hot core.

To quantify whether the water emission arises from the disk or the hot core, the integrated flux densities as expected to arise from the disk are shown in Fig. 6.7 (far right). For the adopted physical models, disks with masses $M_{\rm d} \geq 0.2\ M_\odot$ with accretion rates of a few times $10^{-5}\ M_\odot$ yr^{-1} can also reproduce the water emission without the hot core. However, as shown in Fig. 6.7, most of the emission arises from the hot core assuming a constant water abundance of 10^{-4} with respect to H_2.

The best cases for an actively accreting embedded disk scenario are IRAS4A and IRAS4B. More detailed modelling of their physical structure at < 100 AU radius is required to further constrain the relation between disk accretion (envelope to disk) and stellar accretion rate (disk to star). Mottram et al. (2013) suggests that the infall rate from the large-scale envelope toward IRAS4A at 1000 AU to be $\sim 10^{-4}\ M_\odot$ yr^{-1}. For the cases of disk masses between 0.2–0.5 $M_\odot$, the disk must also process the material at similar rate (within a factor of 10), which is consistent with the models presented here.

6.4.4 Connecting to the young solar nebula

It is thought that the disk out of which the solar system formed (the solar nebula) was initially hot enough to vaporize all material inherited from the collapsing cloud into atoms, then into solids according to a condensation sequence as the nebula cools (Lewis 1974; Grossman & Larimer 1974). Evidence for energetic processing and subsequent condensation comes from meteoritic data collected in the inner solar system (see Kerridge & Matthews 1988; Scott 2007; Apai & Lauretta 2010,for reviews). After the refractory phases have formed, more volatile species such as ices can also condense at larger distances from the young Sun, with the ice composition depending on the temperature and pressure as well as the elemental abundance ratios (e.g., Lunine et al. 1991; Owen & Bar-Nun 1993; Mousis et al. 2009; Pontoppidan et al. 2014). Using cooling curves appropriate for the solar nebula, models show that various ices including H_2O, CH_3OH, NH_3 and CO_2 ice form by condensation out of warm gas out to at least 20 AU (Mousis et al. 2012; Marboeuf et al. 2014). This condensation process is important to explain the composition of volatiles in the atmospheres of solar-system giant planets and comets.

Where and when does this heating and condensation in the disk actually occur? The above processes are usually discussed in the context of protoplanetary disks where the envelope has dissipated and where the water snowline is eventually at a few AU once the disk has cooled.

However, neither observations nor models of disks around solar-mass T-Tauri stars show any evidence that disks are as warm as required above to have condensation happening out to 20 AU (Beckwith et al. 1990; D'Alessio et al. 1998; Dullemond et al. 2007). The results from this paper indicate that instead such a hot disk may be more common in the early stages of disk formation during the *embedded* phase. The disk is then expected to have the high accretion rates which provide the necessary additional heating. Furthermore, the high accretion rates necessary to push the midplane snowlines to 20 AU and beyond tend to occur for only a short time (e.g., Vorobyov 2009). Most volatiles including H_2O, CH_3OH, CO_2 and CO presented here will then be in the gas-phase within this 20–30 AU radius through sublimation of ices. Shortly after, the volatiles re-condense as the accretion rate decreases, with the process controlled by the freeze-out timescale. The inclusion of the gas motions (radially and vertically) and kinetics does not allow for instantaneous re-condensation, thus some gas-phase volatiles should remain near the snowline (Lewis & Prinn 1980; Ciesla & Cuzzi 2006).

A related question is whether the volatiles that are incorporated into planetesimals and eventually planets and icy bodies in the critical 5–30 AU zone are then *inherited* or *reset* during the disk formation process. Evolutionary models by Visser et al. (2009) and Visser et al. (2011) suggest that strongly bound ices such as H_2O are largely pristine interstellar ices in the outer disk, whereas more volatile species can have sublimated, recondensed and reprocessed several times on their way to the inner disk. However, these models have not included internal viscous dissipation as an additional heating source. A warmer early disk can facilitate ice evolution and formation of complex organic molecules in the temperature regime between 20–40 K (Garrod et al. 2008; Nomura et al. 2009; Walsh et al. 2014; Drozdovskaya et al. 2014). Our results including the accretion heating indicate that significant ice re-processing may occur out to larger radii than thought before, well in the comet formation zone. Such a *reset* scenario is supported by the meteoritic data from the inner few AU, but the fraction of material that is reset at larger (e.g. Pontoppidan et al. 2014).

6.5 Summary and conclusions

Two-dimensional embedded disk models have been presented to investigate the location of the snowlines of H_2O, CO_2 and CO. The dust temperature structure is calculated using the 3D dust radiative transfer code RADMC3D with a central heating source ($L_\star + L_{\rm visc}$). An additional heating term from an actively accreting disk has been added through a diffusion approximation. The main parameters that are explored in this paper are $L_\star$, envelope mass, disk radius, disk mass, and disk accretion rate. In addition, the extent of the snowline and optically thin water emission are compared with observations toward three deeply embedded low-mass YSOs. The following lists the main results of this paper.

- The midplane water snowline can extend up to ~ 30 AU for a disk accreting at $10^{-4}\ M_\odot\ {\rm yr}^{-1}$. The CO_2 snowline is located at 100 AU for the same accretion rate. Both H_2O and CO_2 can remain in the solid phase at large radii ($R > 100$ AU) in the midplane within the boundaries of an embedded hydrostatic disk.
- CO is largely found to be in the gas phase within the embedded disk independent of accretion rate and disk properties. Some CO could be frozen out at large radii in the midplane for a relatively massive disk ($M_{\rm d} \geq 0.1\ M_\odot$).
- The predicted water snowlines in our actively accreting embedded disk models can explain the water emission within $R < 50$ AU emitted from the combined hot core and the disk (see Fig. 6.4 R).
- The predicted optically thin water emission is consistent with that observed toward

NGC1333 IRAS4A and IRAS4B for $\dot{M} > 10^{-6}$ $M_{\odot}$ yr^{-1} for the adopted disk masses of 0.5 $M_{\odot}$ and 0.2 $M_{\odot}$, respectively. The observed size of water emission can also be explained with a slightly higher accretion rate model with a lower disk mass. The comparison with the observed water emission toward IRAS2A suggests less disk's contribution relative to IRAS4A and IRAS4B. More detailed physical structure models of NGC1333 IRAS4A and IRAS4B are needed to further quantify the disk's contribution to the observed water emission.

- Significant chemical processing is expected to occur in the inner 100 AU region during the disk formation process in Stage 0. Midplane temperatures between 20–40 K are expected to be prevalent up to 100 AU radius, and 100 K out to 30 AU, for typical accretion rates found in the early phases of star formation. During these warm phases, the chemistry inherited from the collapsing cloud could be reset and more complex molecules could form.

In connection to the solar system formation, the young disk is found to be warm enough such that the water vapor can up to the 30 AU radius within the disk. It is important to realize, however, that a hot young solar nebula out to 30 AU can only occur during the deeply embedded phase, not the T Tauri phase of our solar system. Our models predict that most of the optically thin water emission arises within the inner 50 AU radius. Future Atacama Large Millimeter Array (ALMA) observations spatially resolving the inner 50 AU will test the embedded accreting disk models coupled with better physical models for individual sources. This will lead to better understanding of the physical and chemical structure and evolution of disks in the early stages of star formation.

Acknowledgements

We thank Atilla Juhász for providing scripts for generating and analyzing RADMC3D input and output files. We also thank Kees Dullemond for providing RADMC3D. We are grateful to Catherine Walsh for fruitful discussions. This work is supported by the Netherlands Research School for Astronomy (NOVA). Astrochemistry in Leiden is supported by the Netherlands Research School for Astronomy (NOVA), by a Royal Netherlands Academy of Arts and Sciences (KNAW) professor prize, and by the European Union A-ERC grant 291141 CHEMPLAN.

6.A Snowline test

Water snowlines were inferred and compared with results from Min et al. (2011) in Fig. 6.8 using the minimum mass solar nebula (MMSN) model ($\Sigma \propto r^{-1.5}$). The comparison shows that our adopted method reproduces the water snowlines at high accretion rates. For low accretion rates $\dot{M} \leq 10^{-9}$ $M_{\odot}$ yr^{-1}, our values are slightly smaller yet consistent with those reported in literature.

6.B CO_2 and CO gas fraction

The CO_2 and CO gas pressure dependent gas fraction abundance are shown in Fig. 6.9. The range of density and temperature is the same as Fig. 6.1 (R) except for CO. Figures 6.10 and 6.11 show the midplane CO_2 and CO snowlines as a function of luminosity and $R_{\rm d}$ similar to that of Fig. 6.6 for H_2O.

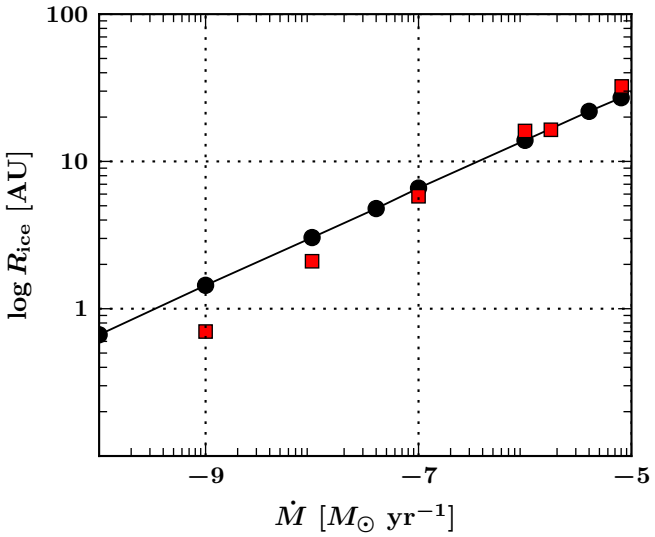

Figure 6.8 — Snowlines for the MMSN disk without an envelope: black circles show the radii calculated with our method and red squares are tabulated values from Min et al. (2011).

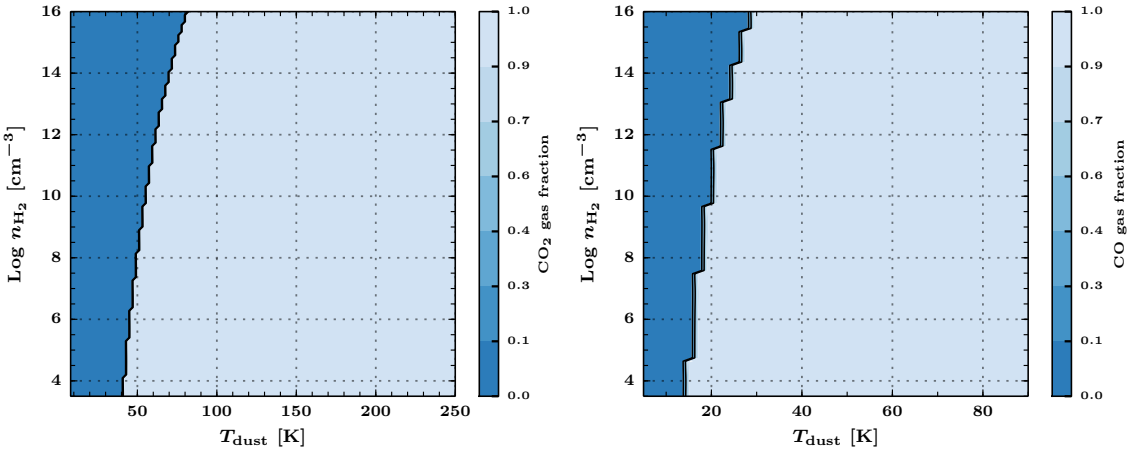

Figure 6.9 — Gas fraction ($n_{\rm gas}/n_{\rm gas} + n_{\rm ice}$) for CO_2 (*Top*) and CO (*Bottom*) as a function of density and temperatures.

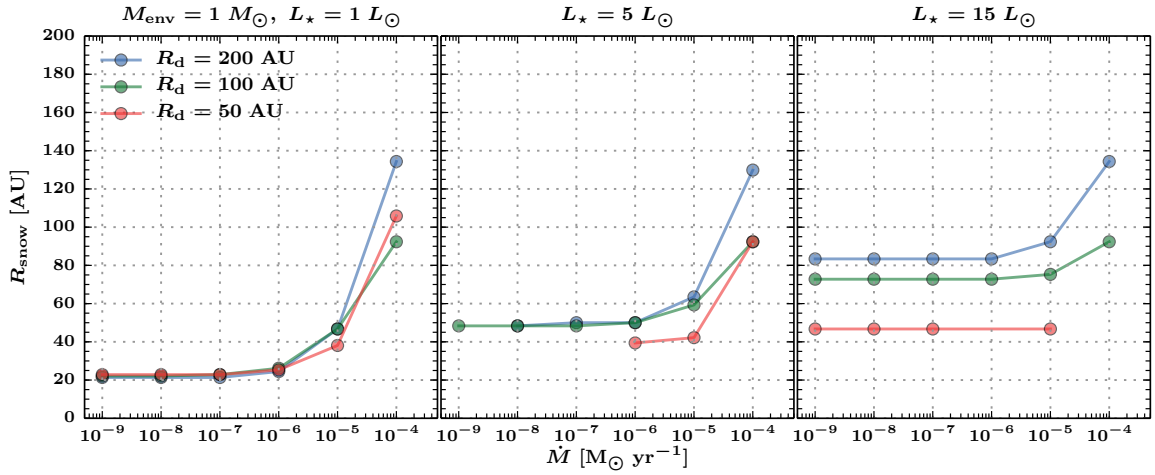

Figure 6.10 — Midplane CO_2 snowline as a function of stellar luminosity, accretion rate, and disk radius. The parameters are similar to that of Fig. 6.6.

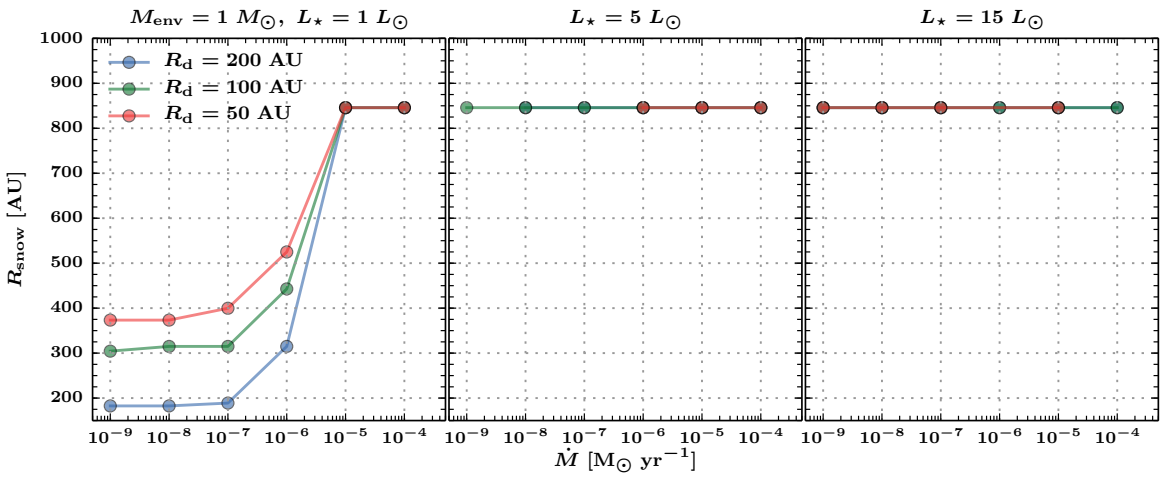

Figure 6.11 — Midplane CO snowline as a function of stellar luminosity, accretion rate, and disk radius. The parameters are similar to that of Fig. 6.6.

Bibliography

Aikawa, Y., Wakelam, V., Garrod, R. T., & Herbst, E. 2008, ApJ, 674, 984

Andrews, S. M., Wilner, D. J., Hughes, A. M., Qi, C., & Dullemond, C. P. 2009, ApJ, 700, 1502

Apai, D. A. & Lauretta, D. S. 2010, Protoplanetary Dust: Astrophysical and Cosmochemical Perspectives (Cambridge Univ. Press, Cambridge)

Bachiller, R. & Tafalla, M. 1999, in NATO ASIC Proc. 540: The Origin of Stars and Planetary Systems, ed. C. J. Lada & N. D. Kylafis, 227

Balbus, S. A. & Hawley, J. F. 1998, Rev. Mod. Phys., 70, 1

Beckwith, S. V. W., Sargent, A. I., Chini, R. S., & Guesten, R. 1990, AJ, 99, 924

Bisschop, S. E., Fraser, H. J., Öberg, K. I., van Dishoeck, E. F., & Schlemmer, S. 2006, A&A, 449, 1297

Brinch, C., Jørgensen, J. K., & Hogerheijde, M. R. 2009, A&A, 502, 199

Burke, D. J. & Brown, W. A. 2010, Phys. Chem. Chem. Phys., 12, 5947

Calvet, N. & Gullbring, E. 1998, ApJ, 509, 802

Calvet, N., Patino, A., Magris, G. C., & D'Alessio, P. 1991, ApJ, 380, 617

Cassen, P. 2001, Meteoritics and Planetary Science, 36, 671

Chiang, E. I. & Goldreich, P. 1997, ApJ, 490, 368

Ciesla, F. J. & Cuzzi, J. N. 2006, Icarus, 181, 178

Crapsi, A., van Dishoeck, E. F., Hogerheijde, M. R., Pontoppidan, K. M., & Dullemond, C. P. 2008, A&A, 486, 245

D'Alessio, P., Calvet, N., & Hartmann, L. 1997, ApJ, 474, 397

D'Alessio, P., Cantö, J., Calvet, N., & Lizano, S. 1998, ApJ, 500, 411

Davis, S. S. 2005, ApJ, 620, 994

de Graauw, T., Helmich, F. P., Phillips, T. G., et al. 2010, A&A, 518, L6

Drozdovskaya, M. N., C., W., R., V., D., H., & van Dishoeck, E. F. 2014, MNRAS, subm.

Dullemond, C. P., Hollenbach, D., Kamp, I., & D'Alessio, P. 2007, in Protostars and Planets V, ed. B. Reipurth, D. Jewitt, & K. Keil (Univ. of Arizona Press, Tucson), 555–572

Dunham, M. M., Stutz, A. M., Allen, L. E., et al. 2014, in Protostars and Planets VI, ed. H. Beuther, C. Dullemond, & T. Henning (Univ. of Arizona Press, Tucson), in press

Fraser, H. J., Collings, M. P., McCoustra, M. R. S., & Williams, D. A. 2001, MNRAS, 327, 1165

Garaud, P. & Lin, D. N. C. 2007, ApJ, 654, 606

Garrod, R. T., Weaver, S. L. W., & Herbst, E. 2008, ApJ, 682, 283

Gibb, E. L., Whittet, D. C. B., Boogert, A. C. A., & Tielens, A. G. G. M. 2004, ApJ, 151, 35

Grossman, L. & Larimer, J. W. 1974, Reviews of Geophysics and Space Physics, 12, 71

Guilloteau, S., Piétu, V., Dutrey, A., & Guélin, M. 2006, A&A, 448, L5

Hartmann, L., Calvet, N., Gullbring, E., & D'Alessio, P. 1998, ApJ, 495, 385

Hasegawa, T. I., Herbst, E., & Leung, C. M. 1992, ApJ, 82, 167

Herczeg, G. J., Karska, A., Bruderer, S., et al. 2012, A&A, 540, A84

Hubeny, I. 1990, ApJ, 351, 632

Hueso, R. & Guillot, T. 2005, A&A, 442, 703

Jørgensen, J. K., Schöier, F. L., & van Dishoeck, E. F. 2005, A&A, 435, 177

Jørgensen, J. K. & van Dishoeck, E. F. 2010a, ApJ, 725, L172

Jørgensen, J. K. & van Dishoeck, E. F. 2010b, ApJ, 710, L72

Jørgensen, J. K., van Dishoeck, E. F., Visser, R., et al. 2009, A&A, 507, 861

Karska, A., Herczeg, G. J., van Dishoeck, E. F., et al. 2013, A&A, 552, A141

Kennedy, G. M. & Kenyon, S. J. 2008, ApJ, 673, 502

Kerridge, J. F. & Matthews, M. S. 1988, Meteorites and the early solar system (Univ. of Arizona Press, Tucson)

King, A. R., Pringle, J. E., & Livio, M. 2007, MNRAS, 376, 1740

Kristensen, L. E., van Dishoeck, E. F., Bergin, E. A., et al. 2012, A&A, 542, A8

Larson, R. B. 2003, Reports on Progress in Physics, 66, 1651

Lecar, M., Podolak, M., Sasselov, D., & Chiang, E. 2006, ApJ, 640, 1115

Lewis, J. S. 1974, Science, 186, 440

Lewis, J. S. & Prinn, R. G. 1980, ApJ, 238, 357

Li, Z.-Y., Banerjee, R., Pudritz, R. E., et al. 2014, in Protostars and Planets VI, ed. H. Beuther, C. Dullemond, & T. Henning (Univ. of Arizona Press, Tucson), in press

Lissauer, J. J. 1987, Icarus, 69, 249

Lodato, G. 2008, New Astron. Rev., 52, 21

Lodders, K. 2004, ApJ, 611, 587

Lunine, J. I., Engel, S., Rizk, B., & Horanyi, M. 1991, Icarus, 94, 333

Madhusudhan, N., Harrington, J., Stevenson, K. B., et al. 2011, Nature, 469, 64

Marboeuf, U., Thiabaud, A., Alibert, Y., Cabral, N., & Benz, W. 2014, ArXiv e-prints

Mathews, G. S., Klaassen, P. D., Juhász, A., et al. 2013, A&A, 557, A132

Min, M., Dullemond, C. P., Dominik, C., de Koter, A., & Hovenier, J. W. 2009, A&A, 497, 155

Min, M., Dullemond, C. P., Kama, M., & Dominik, C. 2011, Icarus, 212, 416

Moses, J. I., Line, M. R., Visscher, C., et al. 2013, ApJ, 777, 34

Mottram, J. C., Kristensen, L. E., van Dishoeck, E. F., et al. 2014, A&A, subm.

Mottram, J. C., van Dishoeck, E. F., Schmalzl, M., et al. 2013, A&A, 558, A126

Mousis, O., Lunine, J. I., Madhusudhan, N., & Johnson, T. V. 2012, ApJ, 751, L7

Mousis, O., Lunine, J. I., Thomas, C., et al. 2009, ApJ, 691, 1780

Murillo, N. M., Lai, S.-P., Bruderer, S., Harsono, D., & van Dishoeck, E. F. 2013, A&A, 560, A103

Nisini, B., Antoniucci, S., Giannini, T., & Lorenzetti, D. 2005, A&A, 429, 543

Nomura, H., Aikawa, Y., Nakagawa, Y., & Millar, T. J. 2009, A&A, 495, 183

Öberg, K. I., Boogert, A. C. A., Pontoppidan, K. M., et al. 2011a, ApJ, 740, 109

Öberg, K. I., Murray-Clay, R., & Bergin, E. A. 2011b, ApJ, 743, L16

Owen, T. & Bar-Nun, A. 1993, Nature, 361, 693

Persson, M. V., Jørgensen, J. K., & van Dishoeck, E. F. 2012,

A&A, 541, A39
Persson, M. V., Jørgensen, J. K., & van Dishoeck, E. F. 2013, A&A, 549, L3
Persson, M. V., Jørgensen, J. K., van Dishoeck, E. F., & Harsono, D. 2014, A&A, 563, A74
Pollack, J. B., Hubickyj, O., Bodenheimer, P., et al. 1996, Icarus, 124, 62
Pontoppidan, K. M., Salyk, C., Bergin, E. A., et al. 2014, in Protostars and Planets VI, ed. H. Beuther, C. Dullemond, & T. Henning (Univ. of Arizona Press, Tucson), in press
Pontoppidan, K. M., Salyk, C., Blake, G. A., & Käufl, H. U. 2010, ApJ, 722, L173
Pringle, J. E. 1981, ARA&A, 19, 137
Qi, C., Öberg, K. I., Wilner, D. J., et al. 2013, Science, 341, 630
Qi, C., Wilner, D. J., Aikawa, Y., Blake, G. A., & Hogerheijde, M. R. 2008, ApJ, 681, 1396
Robitaille, T. P., Whitney, B. A., Indebetouw, R., Wood, K., & Denzmore, P. 2006, ApJ, 167, 256
Ros, K. & Johansen, A. 2013, A&A, 552, A137
Rothman, L., Gordon, I., Barbe, A., et al. 2009, Journal of Quantitative Spectroscopy and Radiative Transfer, 110, 533
Sasselov, D. D. & Lecar, M. 2000, ApJ, 528, 995
Scott, E. R. D. 2007, Annual Review of Earth and Planetary Sciences, 35, 577
Shakura, N. I. & Sunyaev, R. A. 1973, A&A, 24, 337
Stevenson, D. J. & Lunine, J. I. 1988, Icarus, 75, 146
Tobin, J. J., Hartmann, L., Chiang, H.-F., et al. 2012, Nature, 492, 83
Ulrich, R. K. 1976, ApJ, 210, 377
van der Tak, F. F. S., Walmsley, C. M., Herpin, F., & Ceccarelli, C. 2006, A&A, 447, 1011
van Dishoeck, E. F., Bergin, E. A., Lis, D. C., & Lunine, J. I. 2014, in Protostars and Planets VI, ed. H. Beuther, C. Dullemond, & T. Henning (Univ. of Arizona Press, Tucson), in press
van Dishoeck, E. F., Kristensen, L. E., Benz, A. O., et al. 2011, PASP, 123, 138
van Dishoeck, E. F., Thi, W.-F., & van Zadelhoff, G.-J. 2003, A&A, 400, L1
Visser, R., Doty, S. D., & van Dishoeck, E. F. 2011, A&A, 534, A132
Visser, R., Jørgensen, J. K., Kristensen, L. E., van Dishoeck, E. F., & Bergin, E. A. 2013, ApJ, 769, 19
Visser, R., van Dishoeck, E. F., Doty, S. D., & Dullemond, C. P. 2009, A&A, 495, 881
Vorobyov, E. I. 2009, ApJ, 704, 715
Walsh, C., Millar, T. J., & Nomura, H. 2010, ApJ, 722, 1607
Walsh, C., Millar, T. J., Nomura, H., et al. 2014, A&A, 563, A33
Wang, K.-S., van der Tak, F. F. S., & Hogerheijde, M. R. 2012, A&A, 543, A22
White, R. J. & Hillenbrand, L. A. 2004, ApJ, 616, 998
Whitney, B. A., Wood, K., Bjorkman, J. E., & Wolff, M. J. 2003, ApJ, 591, 1049
Williams, J. P. & Cieza, L. A. 2011, ARA&A, 49, 67
Wilson, T. L. & Rood, R. 1994, ARA&A, 32, 191
Zhang, K., Pontoppidan, K. M., Salyk, C., & Blake, G. A. 2013, ApJ, 766, 82